

Generated using the official AMS L^AT_EX template v6.1 two-column layout. This work has been submitted for publication. Copyright in this work may be transferred without further notice, and this version may no longer be accessible.

Quantile Regression, Variational Autoencoders, and Diffusion Models for Uncertainty Quantification: A Spatial Analysis of Sub-seasonal Wind Speed Prediction

GANGLIN TIAN,^a ANASTASE ALEXANDRE CHARANTONIS,^{a,b} CAMILLE LE COZ,^a ALEXIS TANTET,^a AND RIWAL PLOUGONVEN^a

^a *LMD/IPSL, École Polytechnique, Institut Polytechnique de Paris, ENS, Université PSL, Sorbonne Université, CNRS, Palaiseau, 91120, France*

^b *INRIA, Paris, France*

ABSTRACT: This study aims to improve the spatial representation of uncertainties when regressing surface wind speeds from large-scale atmospheric predictors for sub-seasonal forecasting. Sub-seasonal forecasting often relies on large-scale atmospheric predictors such as 500 hPa geopotential height (Z500), which exhibit higher predictability than surface variables and can be downscaled to obtain more localised information. Previous work by Tian et al. (2024) demonstrated that stochastic perturbations based on model residuals can improve ensemble dispersion representation in statistical downscaling frameworks, but this method fails to represent spatial correlations and physical consistency adequately. More sophisticated approaches are needed to capture the complex relationships between large-scale predictors and local-scale predictands while maintaining physical consistency. Probabilistic deep learning models offer promising solutions for capturing complex spatial dependencies. This study evaluates three probabilistic methods with distinct uncertainty quantification mechanisms: Quantile Regression Neural Network that directly models distribution quantiles, Variational Autoencoders that leverage latent space sampling, and Diffusion Models that utilise iterative denoising. These models are trained on ERA5 reanalysis data and applied to ECMWF sub-seasonal hindcasts to regress probabilistic wind speed ensembles. Our results show that probabilistic downscaling approaches provide more realistic spatial uncertainty representations compared to simpler stochastic methods, with each probabilistic model offering different strengths in terms of ensemble dispersion, deterministic skill, and physical consistency. These findings establish probabilistic downscaling as an effective enhancement to operational sub-seasonal wind forecasts for renewable energy planning and risk assessment.

1. Introduction

As the penetration of wind energy in the global energy system increases and annual capacity additions continue to rise, sub-seasonal wind speed forecasts have become increasingly important for optimising turbine maintenance, resource allocation, and grid integration (Luzia et al. 2022; Chen et al. 2019; Tawn et al. 2022; Cassola and Burlando 2012; Chang et al. 2014; White et al. 2017).

Statistical downscaling emerges as an essential bridge between large-scale forecasts and local wind conditions, offering a computationally efficient method for extracting predictability from large-scale circulations into surface wind speed forecasts (Tian et al. 2025; Alonzo et al. 2017; Goutham et al. 2023). However, statistical downscaling methods face a fundamental challenge: they typically produce fields that are too smooth, restricting them to only the portion of the flow that can be estimated from predictors. As a result, they do not appropriately represent the full uncertainty in the system (Orth and Seneviratne 2014; Tian et al. 2025). This limitation is most evident when these statistical downscaling methods are applied to dynamic ensemble forecasts, where the predicted spread under-estimates atmospheric uncertainty, a phenomenon

known as the “under-dispersion problem” (Wilks 2019; Leutbecher 2019). This under-dispersion occurs because deterministic downscaling models only capture the conditional mean of the predictand given predictors, neglecting the conditional variance that represents the inherent uncertainty (Von Storch 1999).

Statistical downscaling must also address the inherent spatial correlation structures within meteorological fields. Wind speed fields exhibit significant spatial dependencies, with studies demonstrating substantial correlations extending up to hundreds of kilometres between sites (Chen et al. 2019; Hill et al. 2011). These correlations reflect the scales of the meteorological features driving the boundary layer winds: fronts at the meso-scale, up to storms on the synoptic scale (Holton and Hakim 2013). These spatial correlations are important for renewable energy applications, as they directly impact power system operations through their representation of regional wind patterns (Sperati et al. 2017). For instance, concurrent production peaks in correlated regions can lead to grid overload (Sperati et al. 2017), while skillful spatial forecasts are essential for transmission system operators managing reserve estimation and grid stability (Davò et al. 2016).

Our previous work (Tian et al. 2025) addressed the under-dispersion issue through stochastic perturbations, adding Gaussian noise derived from statistical model residuals to each grid point independently. While this method

This Work has been submitted to Monthly Weather Review. Copyright in this Work may be transferred without further notice.

Corresponding author: ganglin.tian@lmd.ipsl.fr

contributes to solving the under-dispersion as evaluated by skill scores calculated at each point, it relies on two assumptions that the uncertainty follows a Gaussian distribution and that spatial points are independent. These assumptions oversimplify ensemble uncertainty, particularly in terms of spatial coherence.

Recent advances in probabilistic modelling offer potential solutions to these limitations. Modern approaches such as quantile regression, variational autoencoders (VAEs), and diffusion models provide sophisticated frameworks for uncertainty quantification. Quantile regression enables direct modelling of the conditional distribution without assuming a specific distribution, making it particularly effective for capturing non-Gaussian uncertainty structures in wind speed. Schulz and Lerch (2022) have demonstrated that quantile regression outperforms traditional methods in postprocessing wind speed and temperature forecasts, better capturing the variance of variables across different conditions and skewness of forecast distribution. VAEs have shown promise in wind speed forecasting by learning low-dimensional latent space representations that can encode complex spatial dependencies while generating spatially consistent ensemble members with plausible patterns. VAEs have demonstrated their ability to generate diverse samples that reflect system uncertainties in wind speed prediction (Zhong et al. 2024b). Diffusion models, through their iterative denoising process, can generate diverse yet coherent wind speed fields that preserve the spatial correlations and statistical properties of target fields. Price et al. (2025) and Zhong et al. (2024a) have demonstrated effectiveness in handling signal noise and improving prediction accuracy, particularly in extreme weather conditions. A key consideration for both VAEs and diffusion models is their ability to maintain atmospheric physical realism beyond mere statistical reproduction of historical patterns. These methods move beyond simple Gaussian assumptions and grid-wise independence, potentially addressing both the under-dispersion issue and the need for spatial coherence in ensemble forecasts. However, most existing applications of these methods have focused on short-term or medium-range forecasting horizons (Dong et al. 2023; Price et al. 2025; Lam et al. 2022; Chen et al. 2025; Zhong et al. 2024a,b). While these studies demonstrate the potential of probabilistic models in wind speed prediction, the effectiveness of these methods in capturing and representing spatial uncertainty at sub-seasonal time scales remains unexplored, particularly in statistical downscaling applications where the translation of large-scale predictors to local-scale wind fields introduces additional complexity and uncertainty.

This study examines how these statistical methods capture spatial correlation structures in sub-seasonal wind speed ensembles. Specifically, we aim to: (1) systematically compare how stochastic perturbations, quantile

regression, variational autoencoders, and diffusion models preserve multi-scale spatial dependencies, (2) evaluate whether grid-wise metrics adequately assess the spatial coherence of probabilistic forecasts. This study is structured as follows: Section 2 explains our methodology, outlining the framework for uncertainty quantification and describing the statistical downscaling models, their architectures, and uncertainty representation mechanisms. Section 3 describes the datasets, including ERA5 reanalysis for training and ECMWF sub-seasonal hindcasts for evaluation, as well as preprocessing steps and evaluation metrics. Section 4 analyses model performance on sub-seasonal hindcasts, exploring how forecast skill evolves with lead time through spatially averaged scores, spatial distribution maps, EOF reconstruction, and spectrum analysis. Section 5 discusses our findings in relation to model mechanisms, practical implications, and limitations, and proposes directions for further improvement.

2. Methodology

a. Framework

This study extends our previous work (Tian et al. 2025) by introducing spatial uncertainty quantification methods within the same statistical downscaling framework. While Tian et al. (2025) addressed ensemble under-dispersion through stochastic perturbations, the grid-independent application of these perturbations destroys spatial correlations. This study evaluates three advanced probabilistic methods that better preserve spatial structure: Quantile Regression Neural Network (QNN), Variational Autoencoder-based Neural Network (VNN), and Diffusion-based Neural Network (DNN).

All models are trained on ERA5 reanalysis to learn a probabilistic mapping from 500 hPa geopotential height (\mathbf{X}) to surface wind speed (\mathbf{Y}). We follow the data preprocessing procedures from Tian et al. (2025), including temporal and spatial aggregation and standardisation. Each model optimises specific loss functions detailed in Section 2b. The trained models are then applied to ECMWF ensemble hindcasts for evaluation. For ensemble forecasting, each trained model processes M -member ECMWF ensembles \mathbf{X}^M to generate probabilistic forecasts. QNN produces $P = 10$ quantiles per input member, while SNN, VNN, and DNN generate $P = 20$ independent samples, yielding $P \times M$ total ensemble members for evaluation.

b. Models

Building upon the CNN architecture established by Tian et al. (2025), all probabilistic models employ SmaAt-UNet (Trebing et al. 2021) backbone for consistent feature extraction capabilities. This ensures that performance differences can be attributed primarily to the uncertainty quantification mechanisms rather than variations in underlying

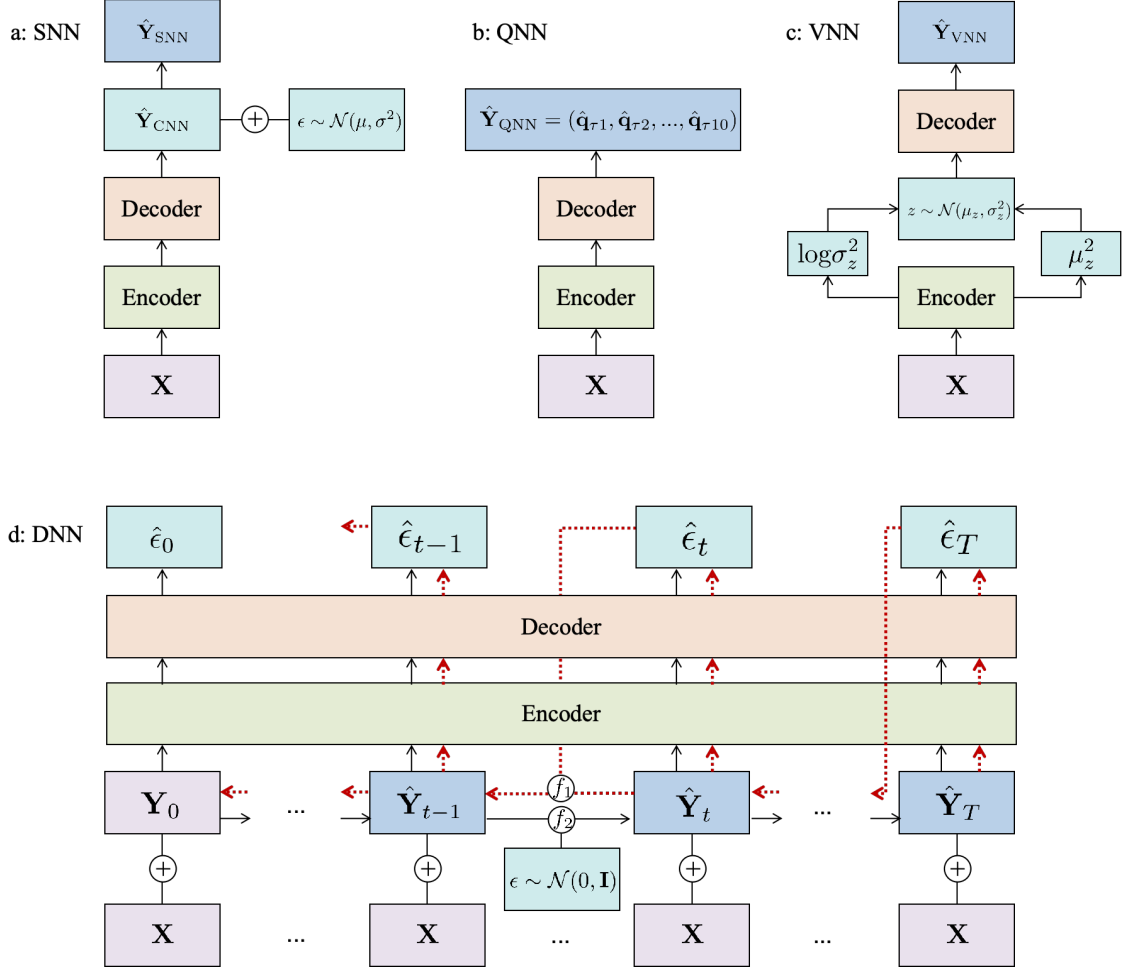


Fig. 1. Architectures of four uncertainty quantification neural networks. (a) Stochastic Neural Network (SNN): SNN incorporates uncertainty by adding gaussian noise $\mathcal{N}(\mu, \sigma^2)$ to deterministic CNN outputs; (b) Quantile Regression Neural Network (QNN): QNN predicts ten specific quantiles ($(\hat{q}_{\tau_1}, \hat{q}_{\tau_2}, \dots, \hat{q}_{\tau_{10}})$) simultaneously to characterise conditional distributions; (c) Variational Autoencoder-based Neural Network (VNN): VNN encodes inputs into a latent probability distribution by outputting mean μ_z and log-variance $\log \sigma_z^2$, then samples from $\mathcal{N}(\mu_z, \sigma_z^2)$ to generate diverse outputs; (d) Diffusion-based Neural Network (DNN): DNN implements a bidirectional diffusion framework with two complementary processes: a forward process (f_2) that progressively adds noise to the clean target field \mathbf{Y}_0 , and a reverse denoising process (f_1) that iteratively removes noise starting from a pure noise state $\hat{\mathbf{Y}}_T \sim \mathcal{N}(0, \mathbf{I})$. During inference, the model predicts noise components $\hat{\epsilon}_t(\hat{\mathbf{Y}}_t, t, \mathbf{X})$ conditioned on both the noisy state and input \mathbf{X} at each timestep, gradually transforming random noise into physically consistent predictions $\hat{\mathbf{Y}}_0$.

spatial feature representation. Each model incorporates specific architectural modifications to implement its particular approach to uncertainty representation. Figure 1 illustrates the four uncertainty representation approaches investigated in this study. Each method represents a distinct theoretical framework for representing conditional distributions, allowing us to systematically evaluate how different uncertainty quantification strategies compare to the established stochastic perturbation approach. For a detailed overview of SmaAt-UNet structure, please refer to the appendix in Tian et al. (2025). Implementation details, including model configuration, hyperparameter optimisation, and training procedures, are provided in Appendix a.

1) QUANTILE REGRESSION-BASED NEURAL NETWORK

Quantile regression extends beyond the conditional expectation $E(\mathbf{Y}|\mathbf{X})$ estimated by traditional regression methods (such as the multiple linear regression and CNN approaches described in Tian et al. (2025)) to directly characterise conditional distributions. Rather than assuming specific distributional forms, this approach estimates the quantiles of the target \mathbf{Y} conditioned on the input \mathbf{X} , denoted as $\hat{q}_\tau(\mathbf{Y}|\mathbf{X})$ at specified quantile levels $\tau \in (0, 1)$, enabling the detection of distributional features such as the asymmetry that are masked by expectation-based methods.

Building upon the CNN architecture established in Tian et al. (2025), QNN in Figure 1b modifies the final convo-

lutional layer of the SmaAt-UNet from single-channel to 10-channel output. Each output channel corresponds to a specific quantile level $\tau_p \in \{5\%, 15\%, \dots, 95\%\}$ for $p = 1, 2, \dots, 10$, enabling simultaneous prediction of all quantiles \hat{q}_τ while sharing feature extraction weights across the encoder-decoder architecture. This 10% interval selection, leading to $P = 10$, provides balanced distributional coverage while maintaining computational efficiency.

QNN is optimised using the loss function:

$$\mathcal{L}_{QNN} = \mathbb{E}_{n,g,p} [\rho_{\tau_p} (\mathbf{Y}_{n,g} - \hat{\mathbf{Y}}_{n,g}^{\tau_p})] \quad (1)$$

where the expectation is taken over all training samples n , grid points g , and quantile levels p . In practice, this expectation is approximated by the empirical average: $\mathcal{L}_{QNN} = \frac{1}{N \cdot G \cdot 10} \sum_{n=1}^N \sum_{g=1}^G \sum_{p=1}^{10} \rho_{\tau_p} (\mathbf{Y}_{n,g} - \hat{\mathbf{Y}}_{n,g}^{\tau_p})$, where N is the number of training samples, G is the number of grid points, and 10 represents the number of quantile levels. Here, $\mathbf{Y}_{n,g}$ is the target value for sample n at grid point g , $\hat{\mathbf{Y}}_{n,g}^{\tau_p}$ is the predicted quantile for a given quantile level τ_p , representing the neural network's estimate of $q_{\tau_p}(\mathbf{Y}|\mathbf{X})$, and $\rho_\tau(u) = u(\tau - \mathbb{I}(u < 0))$ is the quantile loss function, $\mathbb{I}(\cdot)$ is the indicator function. Unlike the MSE optimisation used in traditional regression, this asymmetric loss function assigns different penalties to positive and negative errors. Errors below the target are weighted by τ_p , while errors above are weighted by $(1 - \tau_p)$. By minimising this expected loss across multiple quantile levels, we obtain a comprehensive description of the conditional distribution.

For ensemble forecasting, QNN processes each input ensemble member \mathbf{X}^m to generate ten quantile predictions $\{\hat{\mathbf{Y}}_{n,g}^{\tau_p, m}\}_{p=1}^{10}$. For an input ensemble with M members, this produces a $10 \times M$ -member output ensemble. Rather than maintaining strict quantile ordering across ensemble members, these predictions are treated as exchangeable ensemble members that collectively represent the predictive distribution. This approach prioritises distributional coverage over formal quantile constraints, providing robust uncertainty representation while avoiding quantile crossing issues that can arise in multi-member ensemble contexts.

2) VARIATIONAL AUTOENCODER-BASED NEURAL NETWORK

VAEs provide an alternative approach to uncertainty quantification through latent space sampling. Rather than the direct input-output mapping employed in the CNN approach from Tian et al. (2025), VNN decomposes the prediction task into encoding and decoding stages. The encoder learns to approximate the posterior distribution $q(z|\mathbf{X}, \mathbf{Y})$ of latent features z conditioned on both input predictors and target variables, while the decoder models the conditional distribution $p(\hat{\mathbf{Y}}|z, \mathbf{X})$ for reconstruction given the latent representation and input conditions.

As illustrated in Figure 1c, the VNN architecture modifies the CNN backbone by introducing a bottleneck encoding stage that parameterises latent distributions rather than deterministic features. The encoder outputs mean μ_z and log-variance $\log \sigma_z^2$ vectors representing the parameters of the latent space distribution. During both training and inference, we employ the reparameterisation trick (Kingma et al. 2013) to enable gradient flow: $z = \mu_z + \sigma_z \odot \mathcal{N}(0, I)$, where \odot denotes element-wise multiplication. For a given input, performing P independent sampling operations from this learned latent distribution $\mathcal{N}(\mu_z, \sigma_z^2)$ generates P distinct latent representations, which are then decoded to produce diverse outputs $\hat{\mathbf{Y}}^p$ where $p = 1, 2, \dots, P$. This sampling-based diversity mechanism enables uncertainty quantification by capturing the variability inherent in the latent space.

To optimise both regression accuracy and latent space regularisation, we implement a composite loss function:

$$\mathcal{L}_{VNN} = \mathbb{E}_{n,g} [(\mathbf{Y}_{n,g} - \hat{\mathbf{Y}}_{n,g})^2] + \beta \mathbb{E}_n [\mathcal{L}_{KL}] \quad (2)$$

where the first expectation is taken over all training samples n and grid points g , representing the reconstruction loss between predicted outputs $\hat{\mathbf{Y}}_{n,g}$ and target values $\mathbf{Y}_{n,g}$. The second expectation is taken over training samples, where the Kullback–Leibler (KL) divergence term for samples is:

$$\mathcal{L}_{KL} = -\frac{1}{2} \sum_{i=1}^{d_z} (1 + \log \sigma_{z,i}^2 - \mu_{z,i}^2 - \sigma_{z,i}^2) \quad (3)$$

This β -VAE formulation enables control over the information bottleneck, with higher β values enforcing stronger regularisation but potentially reducing reconstruction fidelity. In practice, both expectations are approximated by empirical averages over the training dataset.

For ensemble forecasting, each input member \mathbf{X}^m undergoes P independent sampling operations in the latent space, generating P distinct predictions that reflect both the learned uncertainty structure and the stochastic sampling process. This approach combines the ensemble uncertainty from the original meteorological ensemble with the regression uncertainty captured by the VAE framework. For an input ensemble with M members, this produces $P \times M$ output ensemble members $\hat{\mathbf{Y}}^{P \times M}$, providing comprehensive uncertainty representation.

3) DIFFUSION-BASED NEURAL NETWORK

Diffusion models establish a reversible mapping between data distributions at different noise levels through two complementary processes: a forward process that gradually adds noise to data until reaching a Gaussian distribution, and a reverse process that systematically removes noise to reconstruct the original data. Unlike QNN's direct

quantile prediction or VNN’s latent space sampling, DNN reframes the prediction task as progressive noise removal conditioned on input atmospheric patterns.

The diffusion framework, illustrated in Figure 1d, consists of two distinct processes operating on the target field \mathbf{Y}_0 (\mathbf{Y}_0 is \mathbf{Y} , where subscript 0 indicates the initial clean state). We define $\hat{\mathbf{Y}}_t$ as the noisy version of the field at diffusion step t , with $\epsilon \sim \mathcal{N}(0, \mathbf{I})$ representing gaussian noise.

The forward diffusion process (denoted as f_2 in Figure 1d) progressively adds noise over T time steps:

$$f_2 : \hat{\mathbf{Y}}_t = \sqrt{\alpha_t} \mathbf{Y}_0 + \sqrt{1 - \alpha_t} \epsilon \quad (4)$$

At each step t , $\hat{\mathbf{Y}}_t$ follows a gaussian distribution with mean $\sqrt{\alpha_t} \mathbf{Y}_0$ and variance $(1 - \alpha_t) \mathbf{I}$. The coefficient $\alpha_t = \prod_{s=1}^t (1 - \beta_s)$ represents the cumulative noise schedule, where β_t increases linearly from β_{start} to β_{end} over T steps:

$$\beta_t = \beta_{\text{start}} + (t - 1) \cdot \frac{\beta_{\text{end}} - \beta_{\text{start}}}{T - 1} \quad (5)$$

The reverse denoising process (denoted as f_1 in Figure 1d) iteratively removes noise to generate predictions:

$$f_1 : \hat{\mathbf{Y}}_{t-1} = \frac{1}{\sqrt{1 - \beta_t}} \left(\hat{\mathbf{Y}}_t - \frac{\beta_t}{\sqrt{1 - \alpha_t}} \hat{\epsilon}_t(\hat{\mathbf{Y}}_t, t, \mathbf{X}) \right) + \sqrt{\beta_t} \epsilon \quad (6)$$

, where $\hat{\epsilon}_t(\hat{\mathbf{Y}}_t, t, \mathbf{X})$ is the model’s predicted noise component at step t given input \mathbf{X} .

During training, the model learns to predict the noise component $\hat{\epsilon}_t$ added at each diffusion step. The loss function optimises noise prediction accuracy across all diffusion steps:

$$\mathcal{L}_{\text{DNN}} = \mathbb{E}_{t,n}[(\epsilon - \hat{\epsilon}_{t,n}(\hat{\mathbf{Y}}_t, t, \mathbf{X}))^2] \quad (7)$$

The expectation is taken over uniformly sampled diffusion time steps and training samples. This formulation trains the model to understand what noise was added at each step of the diffusion process.

For inference, we start with pure noise $\hat{\mathbf{Y}}_T \sim \mathcal{N}(0, \mathbf{I})$ and progressively denoise it through the reverse process. We set the hyperparameters β_{start} and β_{end} (detailed in Appendix a) to ensure a gradual noise injection during training, with β_{start} preserving initial signal integrity and β_{end} ensuring complete noise injection by the final step.

For ensemble forecasting, we implement P independent sampling processes for each input ensemble member \mathbf{X}^m . This generates $P \times M$ output ensemble members for an input ensemble with M members. In our implementation, we set $P = 20$ to maintain a balance between ensemble diversity and computational efficiency.

This iterative denoising approach preserves spatial correlation structures through progressive refinement, addressing the spatial independence limitation identified in

Tian et al. (2025) through different mechanisms than QNN or VNN. The resulting predictions maintain both meteorological ensemble diversity and spatially coherent uncertainty structures.

These probabilistic models quantify regression uncertainty through different mechanisms. QNN directly characterises conditional distribution shapes by predicting multiple quantiles simultaneously. VNN generates diverse outputs through latent space sampling. DNN learns complex conditional distributions through iterative noising and denoising processes. All approaches consider spatial correlations in uncertainty quantification and address the under-dispersion issues in ensemble forecasting.

3. Data and metrics

a. Data

To maintain consistency with Tian et al. (2025), we use the identical data, partitioning strategy, resolution choice, preprocessing methods, and study domains. Input variable (Z500) covers the Europe-Atlantic domain (20° – 80° N, 120° W– 40° E), while the target variable (wind speed at 100 meters, U100) focuses on Europe (34° – 74° N, 13° W– 40° E) during the boreal winter, when Z500 anomalies and circulation-wind correlations are strongest (Laurila et al. 2021). The 100-m height is used as it approximates wind turbine hub heights, making it more relevant for wind energy forecasting than 10-m wind. Both variables are processed to 2.7° spatial resolution and weekly temporal resolution. Wind speed is derived from its components as $U100 = \sqrt{u^2 + v^2}$.

For the training and validation on reanalysis, we use ERA5 reanalysis data from December 1979 to March 2022, obtained from the Climate Data Store. For evaluation on ensembles, we employ 10-member ECMWF extended-range hindcasts with lead times up to 6 weeks, retrieved from the Meteorological Archival and Retrieval System (MARS), covering December 2015 to March 2021 due to licensing constraints.

b. Verification metrics

Building on our previous work (Tian et al. 2025), we assess model performance using both deterministic and probabilistic metrics. Mean Squared Error (MSE) of ensemble mean quantifies deterministic skill, and Continuous Ranked Probability Score (CRPS) and Spread Skill Ratio (SSR) evaluate probabilistic skill.

However, these grid-based metrics fail to capture spatial structure characteristics. Therefore, we introduce complementary spatial analysis techniques, including Empirical Orthogonal Function (EOF) decomposition and energy spectrum analysis. As MSE, CRPS and SSR calculations were detailed in Tian et al. (2025), we focus here on EOF analysis and spectrum analysis.

1) EMPIRICAL ORTHOGONAL FUNCTION ANALYSIS

EOF analysis, also known as principal component analysis in other fields, is a widely used technique for identifying the dominant spatial patterns of variability in meteorological fields (Skittides and Früh 2014; Qin and Dunia 2000; Jiang et al. 2020). EOF modes are ranked strictly by the percentage of variance they explain, not by a direct correspondence to physical spatial scales. The leading (low-order) EOFs capture the dominant patterns of variability, which are often large-scale circulation patterns because such phenomena typically account for the most variance. Conversely, higher-order EOFs represent more detailed and localized spatial structures that contribute progressively less to the total variance. Therefore, this approach evaluates the field's structure through its different modes of variability, which is different from the scale-dependent verification based on physical wavelengths that we address through energy spectrum analysis (next section). For a predictand field $\mathbf{Y} \in \mathbb{R}^{N \times G}$ from ERA5 reanalysis, EOF decomposition yields:

$$\mathbf{Y} = \sum_{k=1}^K \mathbf{PC}_k \cdot \mathbf{EOF}_k \quad (8)$$

where $\mathbf{PC}_k \in \mathbb{R}^N$ represents the temporal coefficients (principal components) of the k -th EOF mode $\mathbf{EOF}_k \in \mathbb{R}^G$. N represents the number of initialisation dates, G is the total number of grid points in the European domain, and K is the maximum number of EOF modes (equal to G in principle).

Our verification framework uses this EOF decomposition in three sequential steps. First, we compute the EOFs from the ERA5 predictand reanalysis fields to establish the reference spatial patterns. Next, we project both the ECMWF ensemble hindcasts and our model outputs onto these reference EOFs to obtain their corresponding principal components $\hat{\mathbf{PC}}_k$. Finally, we reconstruct the regressed fields $\hat{\mathbf{Y}}^{(K')}$ using an increasing number of modes (K'):

$$\hat{\mathbf{Y}}^{(K')} = \sum_{k=1}^{K'} \hat{\mathbf{PC}}_k \cdot \mathbf{EOF}_k \quad (9)$$

For each K' -mode reconstruction, we calculate relative skill scores for both MSE and CRPS metrics, specifically the Mean Squared Skill Score (MSSS) and Continuous Ranked Probability Skill Score (CRPSS), with detailed formulations provided in Appendix b.

2) ENERGY SPECTRUM ANALYSIS

Energy spectrum analysis provides a complementary perspective on spatial verification by quantifying the distribution of variance across different spatial wavelengths (Price et al. 2025; Rasp et al. 2023; Lam et al. 2022). This

approach is particularly useful for identifying systematic biases in the representation of spatial scales, such as excessive smoothing (under-representation of small scales) or noise (over-representation of small scales). For a latitudinal predictand field $\mathbf{Y}_i \in \mathbb{R}^{N \times G_{lon}}$, we compute the zonal energy spectra along the line of constant latitude at latitude index i :

$$S_{\mathbf{Y}_i}(k_z) = \begin{cases} C_\phi |F_{\mathbf{Y}_i}(k_z)|^2, & k_z = 0 \\ 2C_\phi |F_{\mathbf{Y}_i}(k_z)|^2, & k_z = 1, 2, \dots, [G_{lon}/2] \end{cases} \quad (10)$$

where $F_{\mathbf{Y}_i}(k_z) = \frac{1}{G_{lon}} \sum_{j=0}^{G_{lon}-1} \mathbf{Y}_i e^{-i2\pi k_z j / G_{lon}}$, $F_{\mathbf{Y}_i}(k_z) \in \mathbb{R}^N$ is the Fourier transform coefficient for the latitude band, and G_{lon} is the number of longitudinal grid points, $C_\phi = C_0 \cos(\phi_i) \in \mathbb{R}$ with C_0 being the equatorial circumference (equal to $2\pi \times$ Earth radius), and ϕ_i represents the latitude at index i . The factor of 2 accounts for the symmetric contributions from positive and negative frequencies in the real-valued field.

Following Rasp et al. (2023), we average the energy spectra across latitudes to obtain a representative energy spectrum for the European domain, accounting for the latitude-dependent Earth surface area.

$$S_{\mathbf{Y}}(k_z) = \frac{1}{G_{lat}} \sum_i S_{\mathbf{Y}_i}(k_z) \quad (11)$$

where G_{lat} is the number of latitude bands. The energy spectra $S_{\mathbf{Y}}(k_z) \in \mathbb{R}^{N \times G_{lat}}$ provides a measure of the variance in field \mathbf{Y} at each spatial scale corresponding to wavenumber $k_z \in \{0, 1, 2, \dots, [G_{lon}/2]\}$. For our regional European domain, each wavenumber k_z corresponds to a physical wavelength calculated as the inverse of the spatial frequency. This frequency is determined by the wavenumber divided by the longitudinal spacing at each latitude, accounting for the spherical geometry of the Earth. This approach ensures accurate wavelength estimation within our limited spatial domain rather than assuming a global circumference.

By comparing the energy spectra of regressed outputs to those of ERA5 reanalysis, we can systematically evaluate model performance across spatial scales and identify potential biases in the representation of spatial variability. To facilitate comparison, we compute the Relative Energy Spectra Skill score (RESS) score as:

$$\text{RESS}(k_z) = 1 - \frac{S_{\hat{\mathbf{Y}}}(k_z)}{S_{\mathbf{Y}}(k_z)} \quad (12)$$

where $S_{\hat{\mathbf{Y}}}(k_z)$ is the energy spectra of model outputs $\hat{\mathbf{Y}}$ and $S_{\mathbf{Y}}(k_z)$ is the energy spectra of reference (ERA5 reanalysis \mathbf{Y}). This relative energy spectrum skill provides a normalised measure of spectral bias. Values close to 0 indicate perfect agreement between model and reference spectrum. Positive RESS values indicate energy under-

estimation by the model at wavenumber k_z , while negative values indicate energy over-estimation. The magnitude of RESS reflects the degree of bias, with larger absolute values signifying greater discrepancy from the reference spectrum.

3) STATISTICAL SIGNIFICANCE TESTING

To ensure the robustness of our results, we employ bootstrap resampling for statistical significance assessment. Following Tian et al. (2025), we use bootstrap techniques similar to Goddard et al. (2013). For each comparison, we randomly select samples with replacement from model outputs to generate 1000 bootstrap replicates, maintaining the same sample size as the original data.

We calculate verification scores for each bootstrap sample and compute the relative difference $\Delta_r \text{Score} = \frac{\text{Score}(\text{model}_s) - \text{Score}(\text{model}_b)}{\text{Score}(\text{model}_b)} \times 100\% (\%)$ between models. For negatively oriented scores (MSE, CRPS), the proportion of $\Delta_r \text{Score} < 0$ serves as the p -value, while for positively oriented scores, the proportion of $\Delta_r \text{Score} > 0$ provides the p -value. All line plots display median values from bootstrap distributions, while spatial maps indicate statistical significance with different markers.

4. Results

This section evaluates whether grid-wise metrics adequately capture model performance and how different uncertainty quantification methods preserve spatial coherence. The ECMWF ensemble hindcasts are first calibrated using Mean-Variance Adjustment (Goutham et al. 2022, 2023; Manzanas et al. 2019; Tian et al. 2025) to remove systematic bias and adjust ensemble spread, serving as our benchmark. This calibration enables the statistical models to focus on capturing the predictable Z500-U100 relationship. The evaluation proceeds in four parts: spatially averaged scores across lead times (weeks 1-6), spatial distribution of improvements at week 3, EOF analysis, and energy spectrum analysis.

a. Spatially averaged scores

Figure 2 illustrates the spatially averaged MSE, CRPS and SSR of different models across lead weeks. In the first week, all statistical downscaling models exhibit relatively low MSE, as shown in Figure 2a, but they are significantly higher than ECMWF. From week 3 onwards, the MSE of statistical models begins to approach or even slightly exceed ECMWF. This convergence reflects the diminishing benefit of initial conditions in ECMWF hindcasts at longer lead times, where predictability increasingly depends on Z500-U100 relationships that statistical models can effectively capture.

In Figure 2b, CRPS results reveal more pronounced differences. During weeks 1-2, SNN, QNN, and DNN exhibit

similar CRPS performance to their MSE behaviour, underperforming ECMWF. However, from week 3 onwards, these three models achieve better CRPS than ECMWF. In contrast, VNN consistently underperforms ECMWF throughout all lead times.

To understand these CRPS differences, we examine the SSR in Figure 2c. VNN shows substantially lower SSR than other models across all lead times, indicating under-dispersed ensembles that fail to adequately represent forecast uncertainty. While SNN, QNN, and DNN also exhibit under-dispersion ($\text{SSR} < 1$), they remain much closer to the ideal SSR than VNN.

These results indicate that, except for VNN, the statistical models achieve comparable spatially averaged MSE and CRPS performance. VNN's under-dispersion, despite its reasonable mean-state accuracy, suggests biases in its probabilistic representation. This may be attributed to the constraints imposed by the normal distribution assumption in the latent space, which might not fully capture the complex uncertainty structure inherent in wind speed fields.

b. Spatial distribution of improvements

Figure 3 illustrates the spatial distribution of relative improvements in MSE and CRPS for different models compared to calibrated ECMWF at week 3. The spatially averaged MSE improvements are modest, showing the similar performance across models observed in Figure 2. This modest improvement also reflects the limited room for improvement left by ECMWF calibration, which has already removed systematic bias. In contrast, statistical models achieve more substantial CRPS improvements relative to calibrated ECMWF, demonstrating their advantage in uncertainty quantification.

Both MSE and CRPS improvements exhibit similar spatial patterns. Improvements are concentrated in Northern and Western Europe, while performance remains limited over mountainous regions such as the Alps and Balkan Peninsula. This highlights the challenge of representing ensemble uncertainty in areas with complex topography, where topographic influences on wind fields occur at scales finer than those represented in the Z500 predictor field.

c. Skill of reconstructed fields from EOF analysis

Figure 4 assesses model performance in reproducing spatial structures at week 3, based on field reconstructions using a growing number of EOF modes. Using only the first few modes isolates the dominant and high-variance patterns, while including more modes incorporates finer spatial details.

When reconstructing these dominant patterns, all models perform similarly against the ECMWF benchmark, achieving high MSSS and CRPSS scores. Skill scores for most models converge around the 20th EOF mode, indicating a common limit to the predictability of fine-scale

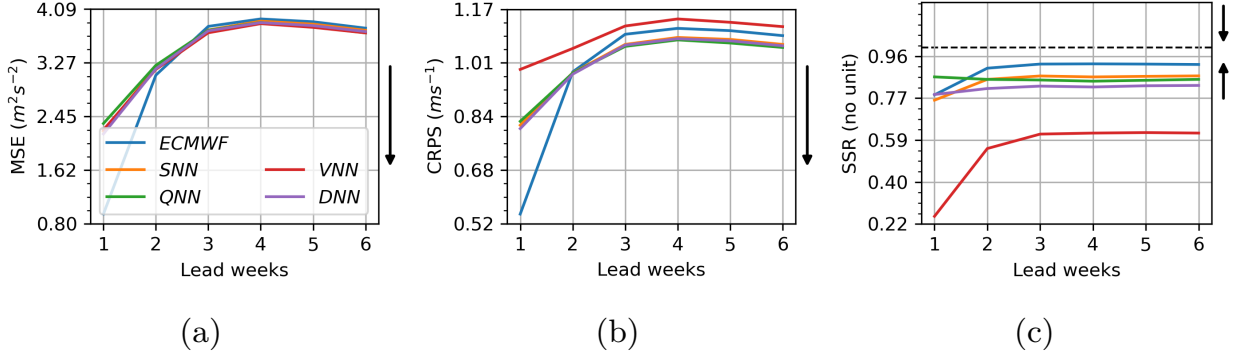


FIG. 2. Spatially averaged MSE, CRPS and SSR of different statistical downscaling models and ECMWF ensemble hindcasts across lead weeks. Black arrows indicate optimal directions: MSE and CRPS (lower is better), SSR (closer to 1, shown as black dashed line, is better).

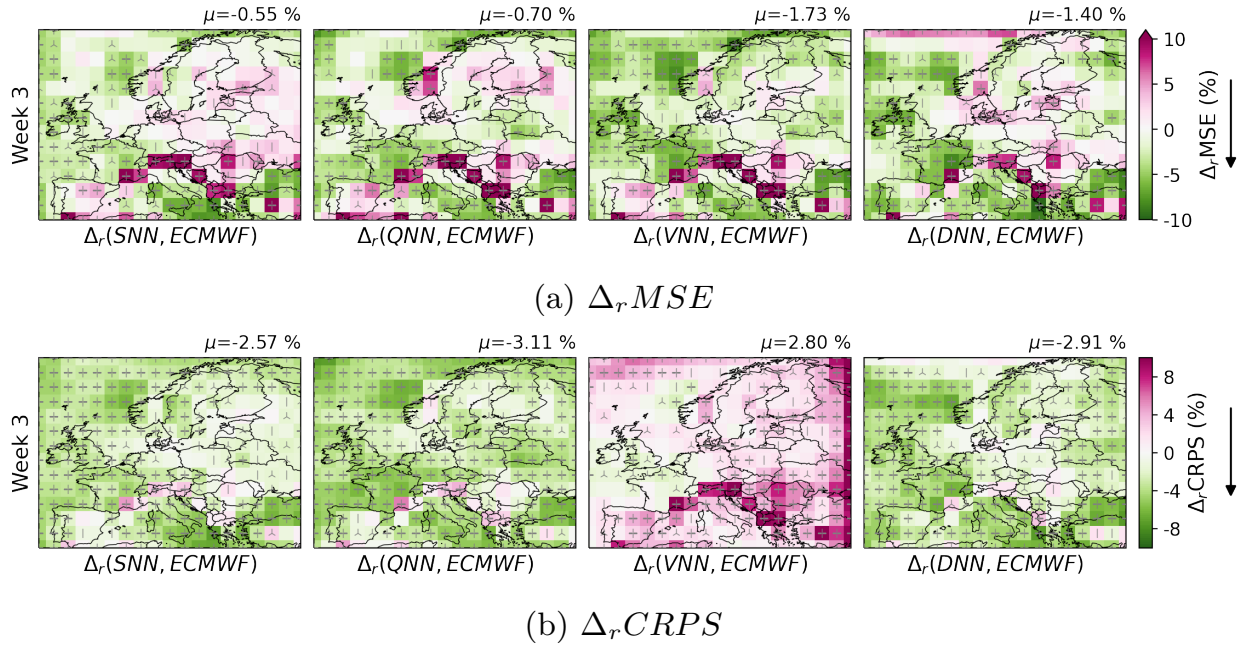


FIG. 3. Spatial distribution of the relative differences in MSE and CRPS (Δ_r MSE and Δ_r CRPS) between SNN, QNN, VNN and DNN compared to Climatology. Green grids indicate improvements (negative values), while pink grids indicate degradation (positive values). Statistical significance is assessed using bootstrap resampling and indicated by symbols overlaid on grid points: “+” denotes significance at $\alpha = 0.01$, “Y” at $\alpha = 0.05$, and “I” at $\alpha = 0.1$. The μ value at the top of each subfigure represents the average relative percentage difference across Europe.

details at this forecast lead time. SNN is an exception. It underperforms in capturing the dispersion of the primary large-scale patterns, as shown by its lower SSR at low mode counts. Yet, its CRPSS improves as more modes are added, rising from 0.04 to 0.06 between the 40th and 266th modes. This is because SNN’s grid-independent perturbations introduce artificial noise, which primarily inflates the variance in higher-order EOFs. Consequently, SNN creates a favourable ensemble spread, but this improvement is an artifact of non-physical noise and it masks the model’s failure to represent large-scale circulation.

d. Energy Spectrum Analysis on Hindcasts

Figure 5 compares the spectra of reanalysis (solid lines) and hindcast (dashed lines) for downscaling, further examining spatial coherence preservation under forecast uncertainty. Note that we use linear wavenumber scaling rather than the conventional log-log representation due to our limited spectral range at 2.7° resolution. The absolute energy spectra (Figure 5a) demonstrate consistency between reanalysis and hindcast environments for the models. The agreement between reanalysis and hindcast energy spectra confirms the robustness of statistical downscaling methods

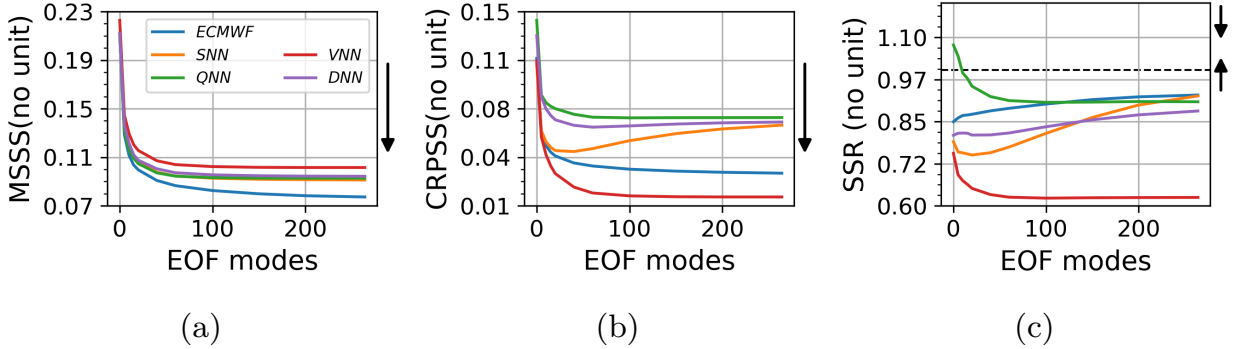


FIG. 4. Skill scores of reconstructed fields by EOF modes for different models on hindcasts. (a) MSSS of ensemble mean, (b) CRPSS, and (c) SSR vary with the number of EOF modes used. Black arrows indicate optimal directions (as in Figure 2): MSSS and CRPSS (higher is better); SSR (closer to 1, shown as black dashed line, is better).

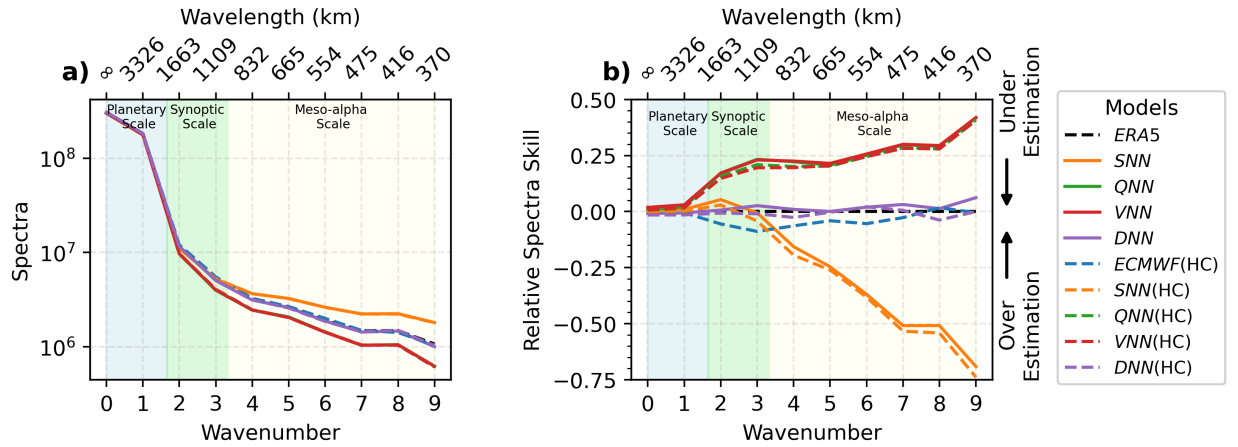


FIG. 5. Energy spectrum analysis on hindcasts at lead week 3 compared with reanalysis data. (a) Absolute energy spectra displayed on a logarithmic scale showing similar patterns between solid lines (reanalysis results) and dashed lines (hindcast results) for corresponding models. (b) Relative energy spectrum skill compared to ERA5 reference, where positive values indicate energy under-estimation and negative values indicate over-estimation. The black arrow and black dashed line at zero indicate the optimal direction: RESS values closer to zero represent better spectral reproduction. The horizontal axis represents zonal wavenumbers with corresponding wavelengths (km).

to forecast uncertainty in the input fields. Nevertheless, this spectral consistency obscures the modest inter-model differences that emerge through relative skill assessment.

The RESS comparison (Figure 5b) reveals model-specific adaptations to forecast uncertainty. ECMWF hindcast shows notable energy over-estimation in the mesoscale range. DNN maintains exceptional multi-scale consistency (RESS \approx 0 across all wavelengths), demonstrating that its diffusion process preserves physical energy distribution even with imperfect inputs. SNN's RESS exhibits a pattern of increase followed by decrease, indicating energy under-estimation at large scales (producing overly smooth fields) and over-estimation at small scales (producing excessively noisy fields). QNN and VNN show nearly identical patterns in both energy spectra and RESS, consistently under-estimating energy and producing overly

smooth wind speed estimates that miss fine-scale variability in wind patterns. The consistency of their RESS between reanalysis and hindcasts indicates that the tendency to produce overly smooth fields is an inherent characteristic of their uncertainty representation mechanisms, rather than a response to input uncertainty.

These results complement the EOF analysis by demonstrating that SNN's apparent skill improvement through stochastic perturbations is artificial and physically unrealistic. They also confirm that DNN provides robust spectral representation under forecast uncertainty, while other models exhibit characteristic limitations that persist or amplify when applied to uncertain inputs.

5. Discussion and Conclusions

This study addressed two questions about uncertainty quantification in sub-seasonal wind speed forecasting: (1) whether grid-wise metrics adequately evaluate probabilistic downscaling methods, and (2) how different uncertainty quantification approaches preserve spatial correlation structures. By comparing stochastic perturbations, quantile regression, variational autoencoders, and diffusion models on ECMWF sub-seasonal hindcasts, we demonstrate the necessity of spatial uncertainty assessment to complement grid-wise evaluation.

a. Uncertainty Mechanisms and Spatial Consistency

All uncertainty quantification methods achieve comparable or superior performance to calibrated ECMWF hindcasts on grid-wise metrics. At week 3, statistical models except VNN show similar MSE with modest CRPS differences, and exhibit lower wind speed skill in complex terrain regions. This apparent skill consistency might suggest that simple stochastic perturbations provide adequate uncertainty quantification for sub-seasonal forecasting. However, grid-wise metrics evaluate only skill at independent grids, failing to capture how uncertainty is spatially structured. This is a limitation for applications where spatial correlations influence aggregate variability, extreme event extent, and regional diversification strategies.

Spatial analyses reveal fundamental differences tied to each method's theoretical foundation. SNN's grid-independent noise creates unrealistic spatial patterns, evidenced by both excessive small-scale energy in the spectrum and artificially inflated variance in higher-order EOF modes. This artifact masks the model's failure to capture the dispersion of dominant large-scale patterns. QNN and VNN both produce overly smooth spatial structures due to their optimisation objectives. QNN's quantile loss optimises marginal distributions at each grid point without spatial correlation constraints, leading to small-scale energy under-estimation. VNN's under-dispersion stems from two interrelated constraints. The KL divergence regularisation toward Gaussian priors limits latent space expressiveness, while the underlying Gaussian assumption cannot fully capture the non-Gaussian complexity inherent in wind field uncertainty. This manifests as both spatial smoothing and insufficient ensemble spread, despite adequate mean-state representation. DNN's iterative denoising operates on entire spatial fields, preserving multi-scale structures through gradual noise refinement that aligns with physical energy cascade processes, achieving near-zero RESS across all wavelengths.

b. Methodological limitations and future directions

This study has several limitations that point toward future research directions. First, all statistical models pre-

sented here only use Z500 as the predictor variable. While this choice was intentional based on preliminary experiments showing that additional variables such as Z50 and SST provided minimal skill improvement, the potential benefits of multi-variate predictors need further investigation for different regions and seasons. Second, the 2.7° spatial resolution balances computational efficiency with meteorological representation while filtering unpredictable noise. However, this coarse resolution limits our ability to resolve fine-scale features in complex terrain. Finer resolution could better capture topographical influences and local circulations, though the computational cost may outweigh marginal skill improvements at sub-seasonal timescales. Third, our temporal independence assumption treats each lead time separately, ignoring temporal correlations in wind evolution. Sequence modeling approaches incorporating temporal dependencies, such as spatio-temporal convolutional networks or recurrent diffusion architectures, could potentially improve performance by better capturing wind field evolution while maintaining physical consistency. Finally, we compared individual uncertainty methods without exploring hybrid or multi-model combinations that might leverage their complementary strengths. Future work should also evaluate model performance for extreme wind events, which are particularly critical for wind energy risk management.

c. Practical applications and implications

Our findings have direct implications for wind energy applications and operational meteorological forecasting. DNN's superior performance in physical consistency makes it particularly suitable for applications where accurate representation of wind field physical properties is crucial (Pickering et al. 2020; Grams et al. 2017). Other models show comparable grid-wise skill, which may suffice for applications that do not require spatial coherence. However, their spatial characteristics impose practical constraints. VNN's insufficient probabilistic skill limits its applicability for risk assessment applications. QNN exhibits small-scale energy under-estimation, potentially degrading performance in local-scale wind forecasting applications.

From a computational perspective, all statistical models require substantially fewer computational resources than dynamical forecasting systems. Inference times range from seconds (SNN, QNN) to several minutes (DNN), with computational complexity increasing approximately in the order $SNN \approx QNN < VNN < DNN$ due to their respective inference mechanisms. However, all methods remain computationally feasible for operational forecasting applications, making forecast skill the primary consideration in model selection.

d. Conclusion

This study demonstrates that capturing spatial correlation structures in uncertainty representation is essential for sub-seasonal wind speed forecasting, extending beyond grid-wise skill assessment. Addressing our two research questions, we show that: (1) grid-wise metrics mask critical differences in spatial uncertainty representation, providing incomplete model assessment when spatial coherence matters, (2) among the four uncertainty quantification approaches, only diffusion models consistently preserve multi-scale spatial dependencies, while stochastic perturbations, quantile regression, and variational autoencoders each exhibit distinct spatial limitations. Quantile regression and variational autoencoders produce overly smooth wind fields with under-estimated small-scale energy. Stochastic perturbations over-estimate energy through spatially uncorrelated noise.

The main contributions of this study include the first systematic comparison of the four modern uncertainty representation methods in statistical downscaling and sub-seasonal wind speed ensemble forecasting, proposing a comprehensive evaluation framework combining forecast verification metrics with spatial consistency analysis, and revealing the theoretical connections between uncertainty representation methods and forecast skill. Despite certain methodological limitations such as single predictor use, fixed spatial resolution, and temporal independence assumptions, this study provides the important insight that advancing sub-seasonal statistical forecasting requires moving beyond grid-point accuracy toward evaluating spatial uncertainty representation.

Acknowledgments. This work has been carried out at the Energy4Climate Interdisciplinary Center (E4C) of IP Paris and Ecole des Ponts ParisTech, which is in part supported by 3rd Programme d’Investissements d’Avenir [ANR-18-EUR-0006-02], and by the Foundation of Ecole polytechnique (Chaire “Défis Technologiques pour une Énergie Responsable” financed by TotalEnergies).

Data availability statement. The ERA5 reanalysis data used in this study are available from the Climate Data Store (<https://cds.climate.copernicus.eu>). The ECMWF extended-range forecast data were obtained through the Meteorological Archival and Retrieval System with an institutional license. Researchers interested in sub-seasonal forecasts and hindcasts can access related datasets through the ECMWF S2S project (<https://www.ecmwf.int/en/research/projects/s2s>). The code used in this study, including the specific configuration of the SmaAt-UNet structure, is available at our GitHub repository: <https://github.com/TIANGANGLIN/s2s-spatial-correlation>.

APPENDIX

a

a. Implementation details

This appendix provides detailed information on the implementation of the probabilistic models described in Section 2b, including training framework and hyperparameter optimisation strategies. While the main text focuses on the theoretical foundations and mathematical formulations of each model, here we elaborate on the practical considerations necessary for reproducing our experimental results.

1) TRAINING FRAMEWORK

Our training procedures build upon the training framework established in Tian et al. (2025), extending the nested cross-validation framework to accommodate advanced spatial uncertainty quantification. We maintained the same data partitioning, preprocessing steps, and validation strategy while adapting the training process for probabilistic modelling.

All these models were trained using the Adam optimiser (Kingma and Ba 2014) to maintain consistency with Tian et al. (2025). However, model-specific learning rate schedules were implemented to accommodate the varying complexity of different probabilistic formulations. Training enhancements implemented in Tian et al. (2025), including the Gaussian noise data augmentation strategy ($\sigma = 0.1$), were maintained to ensure consistency and enable direct performance comparison.

2) HYPERPARAMETER OPTIMISATION

TABLE A1. Model-specific hyperparameter configurations for probabilistic approaches

Model	Hyperparameters
QNN	Learning rate: $\log \mathcal{U}(10^{-6}, 10^{-1})$ Weight decay: $\log \mathcal{U}(10^{-6}, 10^{-1})$
VNN	Learning rate: $\log \mathcal{U}(10^{-6}, 5 \times 10^{-2})$ Weight decay: $\log \mathcal{U}(10^{-6}, 10^{-1})$ Latent dimension (d_z): {32, 64, 128, 256, 512, 1024} KL weight (β): $\log \mathcal{U}(10^{-4}, 2 \times 10^3)$ Skip connections: With or without for each layer
DNN	Learning rate: $\log \mathcal{U}(10^{-6}, 10^{-1})$ Weight decay: $\log \mathcal{U}(10^{-6}, 10^{-1})$ Noise start (β_{start}): $\log \mathcal{U}(10^{-6}, 10^{-3})$ Noise end (β_{end}): $\log \mathcal{U}(10^{-2}, 2 \times 10^{-1})$ Diffusion steps (T): {100, 200, ..., 1000} Time embedding (d_t): {128, 192, 256, ..., 512} DDIM steps: {10, 15, 20, ..., 80} Randomness: {0.0, 0.5, 1.0} Temperature: {0.5, 1.0, 1.5, 2.0}

For hyperparameter optimisation, we employed Optuna (Akiba et al. 2019) with CRPS as the primary optimisation

metric, representing a methodological extension from the MSE-based optimisation in Tian et al. (2025). This change reflects the essential capability of our models to generate probabilistic outputs from deterministic inputs: VNN and DNN maintain consistency with Tian et al. (2025) by generating $P = 20$ probabilistic realisations per input Z500 member, while QNN produces 10 quantiles per input member to represent the conditional distribution. The optimisation process involved 400 trials for each model type using Optuna’s Tree-structured Parzen Estimator (TPE) sampler, which adaptively focused the search on promising regions of the hyperparameter space, ensuring fair comparison across different uncertainty quantification approaches. Table A1 summarises the hyperparameter spaces for each probabilistic model. The increasing complexity from QNN to DNN reflects the different theoretical foundations and uncertainty representation mechanisms of each approach.

The QNN architecture requires optimisation of only standard neural network hyperparameters due to its direct quantile prediction approach. As detailed in Table A1, QNN’s hyperparameter space includes learning rate and weight decay, both sampled from log-uniform distributions ($\log \mathcal{U}$). This relative simplicity compared to other probabilistic methods reflects QNN’s straightforward architectural modification of the established CNN framework.

VNN introduces variational-specific hyperparameters beyond standard neural network parameters. The latent dimension d_z controls the information bottleneck critical for balancing reconstruction fidelity with regularisation, while the KL weight β implements the β -VAE framework. Skip connections configuration determines encoder-decoder information flow, with various connectivity patterns explored during hyperparameter optimisation to maintain spatial coherence while enabling effective latent space learning.

DNN exhibits the highest hyperparameter complexity due to its iterative nature. The noise schedule parameters β_{start} and β_{end} define the linear noise scheduling described above, controlling the forward diffusion process. The time embedding dimension d_t provides sufficient capacity for distinguishing different denoising stages in the iterative reverse process. Additional parameters control the trade-off between sampling speed and quality during inference.

b. Skill Scores

The metrics described in the previous subsections provide absolute measures of forecast performance. However, for model comparison and practical interpretation, it is essential to evaluate performance relative to reference forecasts. Skill scores provide this normalised assessment by expressing model performance as relative improvement over a baseline, typically climatology.

The general form of a skill score is defined as:

$$\text{Skill Score} = 1 - \frac{\text{Score}_{\text{model}}}{\text{Score}_{\text{ref}}} \quad (\text{A1})$$

where a perfect forecast yields a skill score of 1, no improvement over the reference yields 0, and performance worse than the reference yields negative values. This skill score form applies consistently across the deterministic, probabilistic, and spatial metrics employed in this thesis.

The Mean Squared Skill Score (MSSS) quantifies relative improvement in forecast accuracy:

$$\text{MSSS} = 1 - \frac{\text{MSE}_{\text{model}}}{\text{MSE}_{\text{ref}}} \quad (\text{A2})$$

Similarly, the Continuous Ranked Probability Skill Score (CRPSS) evaluates relative improvement in probabilistic forecast quality:

$$\text{CRPSS} = 1 - \frac{\text{CRPS}_{\text{model}}}{\text{CRPS}_{\text{ref}}} \quad (\text{A3})$$

References

Akiba, T., S. Sano, T. Yanase, T. Ohta, and M. Koyama, 2019: Optuna: A next-generation hyperparameter optimization framework. *Proceedings of the 25th ACM SIGKDD International Conference on Knowledge Discovery and Data Mining*.

Alonzo, B., H.-K. Ringjob, B. Jourdier, P. Drobinski, R. Plougonven, and P. Tankov, 2017: Modelling the variability of the wind energy resource on monthly and seasonal timescales. *Renewable energy*, **113**, 1434–1446.

Cassola, F., and M. Burlando, 2012: Wind speed and wind energy forecast through kalman filtering of numerical weather prediction model output. *Applied energy*, **99**, 154–166.

Chang, W.-Y., and Coauthors, 2014: A literature review of wind forecasting methods. *Journal of Power and Energy Engineering*, **2** (04), 161.

Chen, J., K. Höhlein, and S. Lerch, 2025: Learning low-dimensional representations of ensemble forecast fields using autoencoder-based methods. *arXiv preprint arXiv:2502.04409*.

Chen, Y., S. Zhang, W. Zhang, J. Peng, and Y. Cai, 2019: Multifactor spatio-temporal correlation model based on a combination of convolutional neural network and long short-term memory neural network for wind speed forecasting. *Energy Conversion and Management*, **185**, 783–799.

Davò, F., S. Alessandrini, S. Sperati, L. Delle Monache, D. Airoldi, and M. T. Vespucci, 2016: Post-processing techniques and principal component analysis for regional wind power and solar irradiance forecasting. *Solar Energy*, **134**, 327–338.

Dong, X., Z. Mao, Y. Sun, and X. Xu, 2023: Short-term wind power scenario generation based on conditional latent diffusion models. *IEEE Transactions on Sustainable Energy*, **15** (2), 1074–1085.

Goddard, L., and Coauthors, 2013: A verification framework for interannual-to-decadal predictions experiments. *Climate Dynamics*, **40**, 245–272.

Goutham, N., R. Plougonven, H. Omrani, S. Parey, P. Tankov, A. Tantet, P. Hitchcock, and P. Drobinski, 2022: How skillful are the european subseasonal predictions of wind speed and surface temperature? *Monthly Weather Review*, **150** (7), 1621–1637.

Goutham, N., R. Plougouven, H. Omrani, A. Tantet, S. Parey, P. Tankov, P. Hitchcock, and P. Drobinski, 2023: Statistical downscaling to improve the subseasonal predictions of energy-relevant surface variables. *Monthly Weather Review*, **151** (1), 275–296.

Grams, C. M., R. Beerli, S. Pfenninger, I. Staffell, and H. Wernli, 2017: Balancing europe's wind-power output through spatial deployment informed by weather regimes. *Nature climate change*, **7** (8), 557–562.

Hill, D. C., D. McMillan, K. R. Bell, and D. Infield, 2011: Application of auto-regressive models to uk wind speed data for power system impact studies. *IEEE Transactions on Sustainable Energy*, **3** (1), 134–141.

Holton, J. R., and G. J. Hakim, 2013: *An introduction to dynamic meteorology*, Vol. 88. Academic press.

Jiang, Y., D. Cooley, and M. F. Wehner, 2020: Principal component analysis for extremes and application to us precipitation. *Journal of Climate*, **33** (15), 6441–6451.

Kingma, D. P., and J. Ba, 2014: Adam: A method for stochastic optimization. *arXiv preprint arXiv:1412.6980*.

Kingma, D. P., M. Welling, and Coauthors, 2013: Auto-encoding variational bayes. Banff, Canada.

Lam, R., and Coauthors, 2022: Graphcast: Learning skillful medium-range global weather forecasting. *arXiv preprint arXiv:2212.12794*.

Laurila, T. K., V. A. Sinclair, and H. Gregow, 2021: Climatology, variability, and trends in near-surface wind speeds over the north atlantic and europe during 1979–2018 based on era5. *International Journal of Climatology*, **41** (4), 2253–2278.

Leutbecher, M., 2019: Ensemble size: How suboptimal is less than infinity? *Quarterly Journal of the Royal Meteorological Society*, **145**, 107–128.

Luzia, G., A. N. Hahmann, and M. J. Koivisto, 2022: Evaluating the mesoscale spatio-temporal variability in simulated wind speed time series over northern europe. *Wind Energy Science*, **7** (6), 2255–2270.

Manzanas, R., J. M. Gutiérrez, J. Bhend, S. Hemri, F. J. Doblas-Reyes, V. Torralba, E. Penabad, and A. Brookshaw, 2019: Bias adjustment and ensemble recalibration methods for seasonal forecasting: A comprehensive intercomparison using the c3s dataset. *Climate Dynamics*, **53**, 1287–1305.

Orth, R., and S. I. Seneviratne, 2014: Using soil moisture forecasts for sub-seasonal summer temperature predictions in europe. *Climate dynamics*, **43**, 3403–3418.

Pickering, B., C. M. Grams, and S. Pfenninger, 2020: Sub-national variability of wind power generation in complex terrain and its correlation with large-scale meteorology. *Environmental Research Letters*, **15** (4), 044025.

Price, I., and Coauthors, 2025: Probabilistic weather forecasting with machine learning. *Nature*, **637** (8044), 84–90.

Qin, S. J., and R. Dunia, 2000: Determining the number of principal components for best reconstruction. *Journal of process control*, **10** (2-3), 245–250.

Rasp, S., and Coauthors, 2023: Weatherbench 2: A benchmark for the next generation of data-driven global weather models. *arXiv preprint arXiv:2308.15560*.

Schulz, B., and S. Lerch, 2022: Machine learning methods for postprocessing ensemble forecasts of wind gusts: A systematic comparison. *Monthly Weather Review*, **150** (1), 235–257.

Skittides, C., and W.-G. Früh, 2014: Wind forecasting using principal component analysis. *Renewable Energy*, **69**, 365–374.

Sperati, S., S. Alessandrini, and L. Delle Monache, 2017: Gridded probabilistic weather forecasts with an analog ensemble. *Quarterly Journal of the Royal Meteorological Society*, **143** (708), 2874–2885.

Tawn, R., J. Browell, and D. McMillan, 2022: Subseasonal-to-seasonal forecasting for wind turbine maintenance scheduling. *Wind*, **2** (2), 260–287.

Tian, G., C. L. Coz, A. A. Charantonis, A. Tantet, N. Goutham, and R. Plougouven, 2025: Improving subseasonal wind speed forecasts in europe with a nonlinear model. *Monthly Weather Review*, **153** (9), 1761–1779.

Trebing, K., T. Stanczyk, and S. Mehrkanoon, 2021: Smaat-unet: Precipitation nowcasting using a small attention-unet architecture. *Pattern Recognition Letters*, **145**, 178–186.

Von Storch, H., 1999: On the use of “inflation” in statistical downscaling. *Journal of Climate*, **12** (12), 3505–3506.

White, C. J., and Coauthors, 2017: Potential applications of subseasonal-to-seasonal (s2s) predictions. *Meteorological applications*, **24** (3), 315–325.

Wilks, D. S., 2019: *Statistical Methods in the Atmospheric Sciences*. 4th ed., Elsevier, Amsterdam, <https://doi.org/10.1016/C2017-0-03921-6>.

Zhong, X., L. Chen, J. Liu, C. Lin, Y. Qi, and H. Li, 2024a: Fuxi-extreme: Improving extreme rainfall and wind forecasts with diffusion model. *Science China Earth Sciences*, 1–13.

Zhong, X., and Coauthors, 2024b: Fuxi-ens: A machine learning model for medium-range ensemble weather forecasting. *arXiv preprint arXiv:2405.05925*.